Monopole transitions to cluster states in ^{10}Be and ^{9}Li

Yoshiko Kanada-En'yo
Department of Physics, Kyoto University, Kyoto 606-8502, Japan

Isoscalar monopole transitions from the ground states to cluster states in ^{10}Be and ^{9}Li are investigated with ^{6}He$+\alpha$ and ^{6}He$+t$ cluster models, respectively. In ^{10}Be, significant monopole strengths to ^{6}He$+\alpha$ cluster resonances of ^{10}Be$(0^+_{3,4})$ above the α-decay threshold are obtained, whereas those to ^{6}He$+t$ cluster resonances in ^{9}Li are not enhanced because of the large fragmentation of the strengths in the corresponding energy region. The monopole transition to ^{10}Be(0^+_2) having the molecular orbital structure is relatively weak compared with those to ^{6}He$+\alpha$ cluster resonances. Monopole strength distributions do not directly correspond to distributions of ^{6}He$(0^+)+\alpha$ and ^{6}He$(0+)+t$ components but they reflect component of the deformed ^{6}He cluster with a specific orientation, which is originally embedded in the ground state.

arXiv:1604.01453v1 [nucl-th] 6 Apr 2016

I. INTRODUCTION

In this decade, various exotic cluster states have been discovered in neutron-rich nuclei. Neutron-rich Be isotopes are typical examples, in which a variety of cluster structures appear in the ground and excited states (for example, Refs. [1–4] and references therein). In Be isotopes, low-lying states are understood by a molecular orbital picture where valence neutrons in molecular orbitals around a 2α core are considered [1, 3–28]. In highly excited states above the He+He threshold energy, dinuclear-type He+He resonances (cluster resonances) are expected to appear as suggested in ^{10}Be and ^{12}Be [1, 3, 4, 17, 19–49].

The coexistence of molecular orbital structures and cluster resonances in ^{12}Be has been intensively studied by experimental and theoretical works. The ground state of ^{12}Be is a largely deformed intruder state, in which two neutrons occupy a longitudinal molecular orbital so-called the σ orbital around the 2α core. Highly excited states observed by ^{6}He$+^{6}$He and ^{8}He$+^{4}$He decays above the threshold energies are regarded as cluster resonances [46–49]. In theoretical studies with the generalized two-center cluster model (GTCM), Ito *et al.* predicted that ^{8}He$+^{4}$He, ^{6}He$+^{6}$He, ^{7}He$+^{5}$He cluster resonances appear in the energy region a few MeV above the threshold energies [4, 24, 26, 27]. They discussed monopole transitions from the ground state to the excited states and showed that the monopole strength to the ^{8}He$+^{4}$He cluster resonance is strongly enhanced. It means that monopole excitations can be a good probe to experimentally observe cluster resonances.

The coexistence of molecular orbital structures and cluster resonances has been also investigated for ^{10}Be. Theoretical works predicted the $K^\pi = 0^+_2$ band constructed by a largely deformed state with a molecular orbital structure having two σ-orbital neutrons around the developed 2α core. In the experimental energy levels, the 0^+_2 state at 6.18 MeV, the 2^+ state at 7.54 MeV, and the 4^+ state at 10.2 MeV are assigned to the $K^\pi = 0^+_2$ band [32, 34, 38, 39], though the spin and parity of the 10.2 MeV state have not been established yet [36]. Above the $K^\pi = 0^+_2$ band, ^{6}He$+\alpha$ cluster resonances have been theoretically predicted [4, 50], however, there is as yet no experimental evidence of cluster resonances above the ^{6}He$+\alpha$ decay threshold in ^{10}Be. There is only an experimental report of a broad resonance in ^{10}B, which is regarded as the mirror state of a ^{6}He$+\alpha$ cluster resonance [51].

In analogy to ^{10}Be, cluster states in excited states of ^{9}Li have been theoretically studied using a ^{6}He$+t$ cluster model by the author and her collaborators [52]. They predicted ^{6}He$(0^+)+t$ cluster resonances in highly excited states above the t-decay threshold, which can be analogous to ^{6}He$(0^+)+\alpha$ cluster resonances in ^{10}Be. It was also shown that molecular orbital structures do not appear in ^{9}Li because molecular orbitals are unfavored around the asymmetric core of $\alpha+t$, differently from ^{10}Be having the symmetric core of 2α.

In the present paper, I investigate monopole excitations from the ground states to excited ^{10}Be(0^+) and ^{9}Li$(3/2^-)$ states. Attention is focused on monopole strengths to cluster resonances to answer a question whether monopole strengths can be probes to observe cluster resonances. For this aim, I adopt the generator coordinate method (GCM) [53] of the ^{6}He$+\alpha$ and ^{6}He$+t$ cluster models performed to investigate cluster states in ^{9}Li and ^{10}Be in the previous work [52]. I reanalyze ^{9}Li$(3/2^-)$ and ^{10}Be(0^+) states while focusing on monopole excitations. The method has been proved to describe well experimental properties of the ground and the second 0^+ bands in ^{10}Be. In the calculation, resonance states are obtained in a bound state approximation. I estimate cluster decay widths of the cluster resonances from approximated reduced width amplitudes at channel radii, and also evaluate them by changing the size of the box boundary. The monopole strengths for transitions from the ground state to excited states are investigated. Cluster components in the ground and excited states are calculated, and their relation to monopole excitations is discussed.

This paper is organized as follows. In section II, I explain the formulation of the present calculation. I show the calculated results in section III and give discussions of cluster structures and monopole excitations in section IV. Finally a summary and an outlook are given in section

V.

II. FORMULATION

A. ^{6}He + $\alpha(t)$ cluster wave functions

The Bloch-Brink (BB) wave functions [54] of ^{6}He + α and ^{6}He + t cluster wave functions are used as done in the previous work [52]. The ^{6}He and $\alpha(t)$ cluster wave functions are written by harmonic oscillator (ho) shell-model wave functions localized at $\boldsymbol{S}_1 = (0, 0, -\frac{A_2}{A}D)$ and $\boldsymbol{S}_2 = (0, 0, +\frac{A_1}{A}D)$, respectively. Here A_1 and A_2 are the mass numbers of two clusters and A is the total mass number $A = A_1 + A_2$. D indicates the distance parameter, which is treated as the generator coordinate in the superposition of basis wave functions. A common width parameter $\nu = 1/2b^2 = 0.235$ fm^{-2} is used for ^{6}He, α, and t clusters.

The α and t clusters are expressed by $(0s)^2_\pi(0s)^2_\nu$ and $(0s)_\pi(0s)^2_\nu$ configurations, respectively. For the ^{6}He cluster, p-shell configurations of two valence neutrons around an α cluster, $(0s)^2_\pi(0s)^2_\nu(0p)^2_\nu$, are used. To express p-shell configurations, I use the hybrid model space of basis wave functions combining ls and jj coupling schemes as done in the previous work. For the configurations favored in the ls coupling scheme, $|p_z, n\uparrow\rangle|p_z, n\downarrow\rangle$ and its rotated configurations are used to take into account ^{6}He$(0^+, 2^+)$ states with the two-neutron intrinsic spin $S_{12} = 0$. For those favored in the jj coupling scheme, $|p_{(+)}, n\uparrow\rangle|p_{(-)}, n\downarrow\rangle$ and its rotated configurations are adopted to take into account ^{6}He$(0^+, 2^+)$ states in the $p^2_{3/2}$ configurations. Here, $p_{(+)}, p_z, p_{(-)}$ stand for the ho p orbits with $l_z = +1, 0, -1$, respectively (l_z is the z-component of the orbital angular momentum $\boldsymbol{l}$). Note that the hybrid model space of these ls coupling and jj coupling configurations for the ^{6}He cluster is equivalent to the full model space of p-shell configurations for ^{6}He$(0^+, 2^+)$.

The ^{6}He + α and ^{6}He + t cluster wave functions projected onto parity and total-angular-momentum eigen states are written as,

$$P^{J\pi}_{MK}|\Phi_\tau(D)\rangle = P^{J\pi}_{MK}\mathcal{A}\{|\psi_{1\tau}(\boldsymbol{S}_1)\rangle|\psi_{2\tau}(\boldsymbol{S}_1)\rangle \times|\phi(\boldsymbol{S}_1)p\uparrow\rangle|\phi(\boldsymbol{S}_1)p\downarrow\rangle|\phi(\boldsymbol{S}_1)n\uparrow\rangle|\phi(\boldsymbol{S}_1)n\downarrow\rangle \times|\phi(\boldsymbol{S}_2)p\uparrow\rangle|\phi(\boldsymbol{S}_2)p\downarrow\rangle|\phi(\boldsymbol{S}_2)n\uparrow\rangle|\phi(\boldsymbol{S}_2)n\downarrow\rangle\} \quad (1)$$

and

$$P^{J\pi}_{MK}|\Phi_\tau(D)\rangle = P^{J\pi}_{MK}\mathcal{A}\{|\psi_{1\tau}(\boldsymbol{S}_1)\rangle|\psi_{2\tau}(\boldsymbol{S}_1)\rangle \times|\phi(\boldsymbol{S}_1)p\uparrow\rangle|\phi(\boldsymbol{S}_1)p\downarrow\rangle|\phi(\boldsymbol{S}_1)n\uparrow\rangle|\phi(\boldsymbol{S}_1)n\downarrow\rangle \times|\phi(\boldsymbol{S}_2)p\uparrow\rangle|\phi(\boldsymbol{S}_2)n\uparrow\rangle|\phi(\boldsymbol{S}_2)n\downarrow\rangle\}. \quad (2)$$

Here $\phi(\boldsymbol{S}_i)$ is the $0s$ wave function shifted to the position $\boldsymbol{S}_i$. $|\psi_{1\tau}(\boldsymbol{S}_1)\rangle$ and $|\psi_{2\tau}(\boldsymbol{S}_1)\rangle$ indicate p-shell orbits for neutron configurations labeled by $\tau = \{a, b, c, d, e, f\}$ of the ^{6}He cluster shifted to $\boldsymbol{S}_1$. Schematic figures for the configurations $\tau = \{a, b, c, d, e, f\}$ are illustrated in Fig. 1.

The ls coupling configurations are given by the configurations $\tau = a$, b, and c, in which two neutron orbits are written by rotated configurations of $|p_y, n\uparrow\rangle_{\boldsymbol{S}_1}|p_y, n\downarrow\rangle_{\boldsymbol{S}_1}$ as

$$|\psi_{1\tau}(\boldsymbol{S}_1)\rangle = \hat{R}_{x,\boldsymbol{S}_1}(\theta)|p_y, n\uparrow\rangle_{\boldsymbol{S}_1}, \quad (3)$$

$$|\psi_{2\tau}(\boldsymbol{S}_1)\rangle = \hat{R}_{x,\boldsymbol{S}_1}(\theta)|p_y, n\downarrow\rangle_{\boldsymbol{S}_1}, \quad (4)$$

with the rotation angle $\theta = \pi/2$, $\theta = \pi/4$, and $\theta = 0$, respectively. Here $\hat{R}_{x,\boldsymbol{S}_1}(\theta)$ is the rotation operator around the x-oriented axis passing through $\boldsymbol{S}_1$.

The $p^2_{3/2}$ configurations in the jj coupling scheme are described by the configurations $\tau = d$, e, and f, in which two neutron orbits are given by rotated configurations of $|p_{(+)}, n\uparrow\rangle_{\boldsymbol{S}_1}|p_{(-)}, n\downarrow\rangle_{\boldsymbol{S}_1}$ as

$$|\psi_{1\tau}(\boldsymbol{S}_1)\rangle = \hat{R}_{x,\boldsymbol{S}_1}(\theta)|p_{(+)}, n\uparrow\rangle_{\boldsymbol{S}_1}, \quad (5)$$

$$|\psi_{2\tau}(\boldsymbol{S}_1)\rangle = \hat{R}_{x,\boldsymbol{S}_1}(\theta)|p_{(-)}, n\downarrow\rangle_{\boldsymbol{S}_1}, \quad (6)$$

where $\theta = \pi/2$, $\theta = \pi/4$, and $\theta = 0$ are chosen for d, e, and f, respectively.

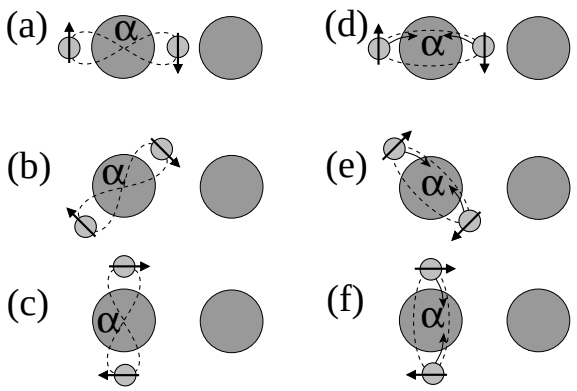

FIG. 1: Schematic figures for configurations (a)-(f) of the ^{6}He cluster in the ^{6}He+t and ^{6}He+α cluster models. Details are described in the text.

In the GCM calculation, the ^{6}He + $\alpha(t)$ cluster wave functions are superposed as

$$|\Psi^{J^\pi_k}_M\rangle = \sum_D \sum_{\tau,K} c^{(J^\pi_k)}_{D,\tau,K} P^{J\pi}_{MK}|\Phi_\tau(D)\rangle, \quad (7)$$

where the coefficients $c^{(J^\pi_k)}_{D,\tau,K}$ are determined by diagonalizing norm and Hamiltonian matrices. I use the generator coordinate $D \le D_{\max}$ and get wave functions for resonances states as bound-state solutions.

The present model space given by the K-projected wave functions of six configurations fully covers all p-shell configurations of 0^+ and 2^+ states of the ^{6}He cluster

located at the inter-cluster distance D. A single configuration has the deformed ^{6}He cluster with a specific orientation and indicates a strong-coupling cluster structure, in which angular momenta of clusters and that of the inter-cluster motion are strongly coupled. At a moderate distance D, the configuration (a) having two neutrons in the longitudinal direction approximately corresponds to the molecular orbital σ^2 structure because of the antisymmetrization effect, which is the dominant component of the ^{10}Be(0_2^+) state consistently with preceding works [4, 6–15, 17, 20, 23]. On the other hand, in the asymptotic region of a large distance D, the system goes to a weak-coupling cluster state, in which the ^{6}He subsystem becomes its energy eigen state with a certain spin I. In the present framework, the transition between strong-coupling to weak-coupling cluster structures is taken into account by the linear combination of configurations (a)-(f) projected to total angular momentum eigen states. The present expression is useful to analyze cluster structures of ^{6}He+$\alpha(t)$ in ^{10}Be(^{9}Li), in particular, in a strong-coupling regime.

Transition between strong-coupling and weak-coupling cluster structures of ^{10}Be was nicely presented by Ito *et al.* [20, 23] using the GTCM, in which molecular orbital configurations are fully taken into account by channel coupling (configuration mixing) of the ^{5}He+^{5}He channel with ^{6}He+α channel. In the present work, I omit the coupling with the ^{5}He+^{5}He channel to save the number of basis wave functions. In spite of omitting the ^{5}He+^{5}He configurations, the present method works well to describe experimental energy spectra of the $K=0_1^+$, $K=2_1^+$, and $K=0_2^+$ bands of ^{10}Be as already shown in the previous work.

In the practical calculation, I express a configuration of the ^{6}He + $\alpha(t)$ wave functions with a single AMD wave function which is given by a Slater determinant of single-particle Gaussian wave packets. General form of the AMD wave functions is described, for example, in Refs. [2, 3, 55].

B. Isoscalar monopole transitions

The isoscalar monopole (ISM) operator $\mathcal{M}(IS0)$ is defined as

$$\mathcal{M}(IS0) \ = \ \sum_i (\boldsymbol{r}_i - \boldsymbol{R})^2, \tag{8}$$

where $\boldsymbol{r}_i$ is the ith nucleon coordinate and $\boldsymbol{R}$ is the center of mass coordinate $\boldsymbol{R} \equiv \sum_i \boldsymbol{r}_i/A$. The ISM strength from the ground state to an excite state (J_k^π) is given by the reduced matrix element of the ISM operator as

$$B(IS0; \text{g.s.} \to J_k^\pi) = \frac{1}{2J+1} |\langle \text{g.s.} || \mathcal{M}(IS0) || J_k^\pi \ \rangle|^2. \tag{9}$$

The energy-weighted sum (EWS) of the ISM strengths is defined as

$$S(IS0) \equiv \sum_k (E_k - E_{\text{g.s.}}) B(IS0; \text{g.s.} \to J_k^\pi), \tag{10}$$

If the interaction commutes with $\mathcal{M}$(IS0), the ISM energy weighted sum rule (EWSR)

$$S(IS0) = \frac{2\hbar^2}{m} A \langle r^2 \rangle_{\text{g.s.}} \tag{11}$$

is satisfied. Here $\langle r^2 \rangle_{\text{g.s.}}$ is the mean-square radius of the ground state and equals to $\langle \text{g.s.} | \mathcal{M}(IS0) | \text{g.s.} \rangle / A$.

III. RESULTS

A. Effective nuclear forces

The effective Hamiltonian consists of the single-particle kinetic terms t_i and two-body forces v_{ij} containing effective nuclear forces and the Coulomb force,

$$H_{\text{eff}} = \sum_i t_i - T_G + \sum_{i<j} v_{ij}, \tag{12}$$

where the kinetic energy T_G of the center of mass motion is subtracted. As for the effective nuclear forces, the Volkov No.2 force [56] is used for the central force, and the spin-orbit term of the G3RS force [57] is adopted for the spin-orbit force, as done in preceding works for ^{10}Be and ^{9}Li structures [10, 13, 14, 52, 58]. The interaction parameters are $(b = h = 0.125, m = 0.60)$ for the Volkov No.2 force and $u_I = -u_{II} = 1600$ MeV for the strength of the spin-orbit force. These are the same parameters as those used in Refs. [52, 58]. The Coulomb force is approximated by seven-range Gaussians.

B. Energy levels of ^{9}Li and ^{10}Be

As described in (7), the ^{6}He + $\alpha(t)$ cluster wave functions $|\Phi_\tau(D)\rangle$ specified by the label τ and the distance parameter D are superposed. In the default GCM calculation, I take the generator coordinate, $D = 1, 2, \cdots, 8$ fm, which corresponds to a bound state approximation. To see resonance features, I also take a larger model space, $D = 1, 2, \cdots, 15$ fm, to examine the effect of coupling with discretized continuum states. The six configurations, τ={a,b,c,d,e,f}, are adopted at each D, and totally $6 \times 8 = 48 (6 \times 15 = 90)$ basis wave functions are superposed in the $D = 1, 2, \cdots, 8$ fm ($D = 1, 2, \cdots, 15$ fm) calculation, which I denote the "$D \le 8$ ($D \le 15$)" calculation. In the $D \le 8$ and $D \le 15$ calculations, the K-mixing is taken into account. In addition, I also perform the GCM calculation with a truncated model space using only the transverse configurations, (c) and (f), denoted the "(c+f)" calculation. In the (c+f) calculation,

the angular momentum projected ^{6}He + $\alpha(t)$ wave functions of the configurations, (c) and (f), with $K = 0(1/2)$ and $D = 1, 2, \cdots, 8$ fm are used.

Figure 2 shows the energy spectra of ^{10}Be(0^+) and ^{9}Li($3/2^-$) obtained by the default $D \leq 8$ calculation. The ^{6}He + α and ^{6}He + t threshold energies are shown by dashed lines. The ^{10}Be($0^+_{3,4}$) and ^{9}Li($3/2^-_{3,4,5}$) states are obtained above the ^{6}He + α and ^{6}He + t threshold energies, respectively. The ^{10}Be(0^+_3) and ^{10}Be(0^+_4) states have relatively larger ^{6}He(0^+) + α and ^{6}He(2^+) + α components, respectively. The ^{9}Li($3/2^+_3$) is dominated by the ^{6}He(0^+) + t component, where as the ^{9}Li($3/2^+_4$) and ^{9}Li($3/2^+_5$) have the dominant ^{6}He(2^+) + t components. The dominant ^{6}He + $\alpha(t)$ components decrease at the boundary, D = 8 fm, and hence these states are regarded as resonance states. Other states higher than the ^{10}Be(0^+_4) and ^{9}Li($3/2^+_5$) states do not show such the resonance feature and are regarded as continuum states. In the low-energy region of ^{10}Be, the 0^+_2 state of ^{10}Be with the molecular σ-orbital structure is obtained below the threshold energy. This state is the band-head state of the $K^\pi = 0^+_2$ band and assigned to the experimental 0^+ state at 6.18 MeV. However, in ^{9}Li, the molecular orbital structure does not appear because the σ-orbital is unfavored around the $\alpha + t$ core because of the asymmetry of the core potential as discussed in the previous work. The ^{9}Li($3/2^-_2$) state obtained below the ^{6}He+t threshold energy is the band-head state of the $K^\pi = 3/2^-$ band.

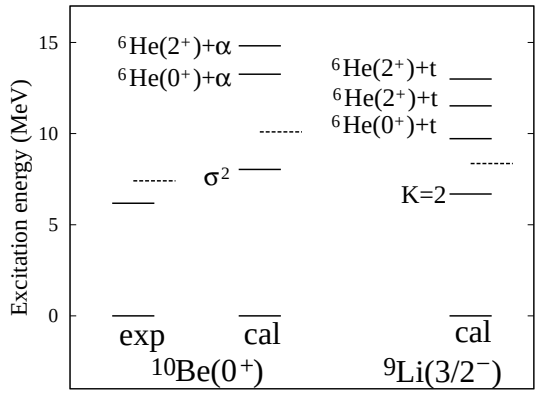

FIG. 2: Energy levels of ^{10}Be(0^+) and ^{9}Li($3/2^-$) obtained by the $D \leq 8$ calculation. The experimental energy levels of ^{10}Be(0^+) are also shown. The ^{6}He + α and ^{6}He + t threshold energies are shown by dashed lines.

In the $D \leq 8$ calculation, the resonance states are obtained as bound state solutions in the model space of $D \leq 8$ fm. I estimate the partial decay widths $\Gamma_{I\otimes J'}$ of the resonance states for ^{6}He(I^+) + $\alpha(t)$ channels with the angular momentum coupling $[I \otimes J']_J$ from the reduced width amplitude $y(a)$ at a channel radius a as described in appendix A. Here J' is the resultant angular momentum of the angular momenta I' and l, where I' is the internal angular momentum of the $\alpha(t)$ cluster and l is the orbital angular momentum for the relative coordinate $\boldsymbol{r}$ between centers of mass of two clusters. For ^{6}He(0^+) + α and ^{6}He(2^+) + α decays of ^{10}Be(0^+), S- and D-wave decays in the $[I \otimes J']_J = [0 \otimes 0]_0$ and $[2 \otimes 2]_0$ channels are calculated, respectively. For ^{6}He(0^+) + t and ^{6}He(2^+) + t decays of ^{9}Li($3/2^-$), I consider P-wave decays in three channels, $[0 \otimes 3/2]_{3/2}$, $[2 \otimes 3/2]_{3/2}$, and $[2 \otimes 1/2]_{3/2}$.

The calculated partial decay widths $\Gamma_{I\otimes J'}$ at channel radii a =5, 6, and 7 fm are shown in Table I. Here, decay energies ($E_{\rm decay}$) are calculated from the theoretical energies of t, α, ^{6}He($0^+, 2^+$), ^{10}Be, and ^{9}Li. The sum $\Gamma_{\rm sum}$ of the partial widths and the dimensionless reduced widths $\theta^2(a) = (a/3)|ay(a)|^2$ are also shown in the table. Here after, I discuss the decay widths calculated at the channel radius that gives the largest $\Gamma_{\rm sum}$ for each state. The calculated width of the ^{10}Be(0^+_3) is $\Gamma_{\rm sum}$ = 1.6 MeV with the dominant ^{6}He(0^+) + α decay and that of the ^{10}Be(0^+_4) is $\Gamma_{\rm sum}$ = 1.0 MeV with comparable partial widths of ^{6}He(0^+) + α and ^{6}He(2^+) + α decays. The calculated widths of the ^{9}Li($3/2^-_3$), ^{9}Li($3/2^-_4$), and ^{9}Li($3/2^-_5$) are $\Gamma_{\rm sum}$ = 0.65, 0.75, and 2.0 MeV, respectively. The ^{9}Li($3/2^-_3$) can decay only in the ^{6}He(0^+) + t channel because the ^{6}He(2^+) + t channel is closed. The ^{9}Li($3/2^-_4$) has comparable partial widths of ^{6}He(0^+) + t and ^{6}He(2^+) + t decays, whereas the ^{9}Li($3/2^-_5$) has dominant ^{6}He(2^+) + t decays.

To see resonance features of these states obtained above the threshold energies, I perform the $D \leq 15$ calculation with the larger model space than that of the $D \leq 8$ calculation. In the model space enlarged from $D \leq 8$ fm to $D \leq 15$ fm, the resonance states $|\Psi^{J^\pi_k}_{D\leq 8}\rangle$, which obtained as bound state solutions in the $D \leq 8$ calculation, couple with discretized continuum states and their components are fragmented in states ($|\Psi^{J^\pi_l}_{D\leq 15}\rangle$) in the $D \leq 15$ calculation. In Fig. 3, I show the squared overlap $|\langle\Psi^{J^\pi_k}_{D\leq 8}|\Psi^{J^\pi_l}_{D\leq 15}\rangle|^2$. The overlap distributions show that the components of the resonance states obtained by the $D \leq 8$ calculation are fragmented into several states in the $D \leq 15$ calculation, whereas those of the ^{10}Be(0^+_2) and ^{9}Li($3/2^+_2$) below the threshold energies are not fragmented. As shown in the figure, the overlap distributions are consistent with the Breit-Wigner distributions at the resonance energies with the widths ($\Gamma_{\rm sum}/2$) obtained by the $D \leq 8$ calculation. This result indicates that the decay widths $\Gamma_{\rm sum}$ estimated by using the reduced width amplitudes are reasonable.

^{6}He + α cluster resonances as well as molecular orbital states in ^{10}Be have been investigated by Ito *et al.* with the GTCM. The GTCM calculation predicted a ^{6}He(2^+) + α resonance at the energy E_r = 3.6 MeV relative to the ^{6}He + α threshold energy and a ^{6}He(0^+) + α state as a broad continuum state in the $E_r = 1 - 4$ region. The present result of the ^{10}Be(0^+_4) with the dominant ^{6}He(2^+) + α component may correspond to the ^{6}He(2^+) + α state of the GTCM. The ^{10}Be(0^+_3) obtained in the present result, which has the dominant ^{6}He(0^+)+α component and a larger width than the ^{10}Be(0^+_4), is likely

to correspond to the ^{6}He$(0^+)+\alpha$ state of the GTCM.

TABLE I: Partial decay widths $\Gamma_{I\otimes J'}$ (MeV) for ^{6}He$(I^+)+\alpha$ of ^{10}Be(0^+) and ^{6}He$(I^+)+t$ of ^{9}Li$(3/2^-)$ obtained by the $D \leq 8$ calculation. $\Gamma_{I\otimes J'}$ for S-wave and D-wave decays in $[0\otimes 0]_0$ and $[2\otimes 2]_0$ of ^{10}Be(0^+) and P-wave decays in $[0\otimes 3/2]_{3/2}$, $[2\otimes 3/2]_{3/2}$, and $[2\otimes 1/2]_{3/2}$ of ^{9}Li$(3/2^-)$ are shown. The sum ($\Gamma_{\rm sum}$) of the partial widths and the dimensionless reduced widths $\theta^2(a) = (a/3)|ay(a)|^2$ are also shown.

	$E_{\rm decay}$ (MeV)	θ^2			$\Gamma_{I\otimes J'}$ (MeV)		
a (fm)		5	6	7	5	6	7
^{6}He$(0^+)+\alpha$ with $[0\otimes 0]_0$							
^{10}Be(0^+_3)	3.2	0.04	0.20	0.38	0.18	0.92	1.55
^{10}Be(0^+_4)	4.7	0.02	0.01	0.10	0.14	0.05	0.54
^{6}He$(2^+)+\alpha$ with $[2\otimes 2]_0$							
^{10}Be(0^+_3)	1.3	0.13	0.12	0.08	0.011	0.02	0.02
^{10}Be(0^+_4)	2.9	0.07	0.19	0.23	0.10	0.34	0.49
^{6}He$(0^+)+t$ with $[0\otimes 3/2]_{3/2}$							
^{9}Li$(3/2^-_3)$	1.4	0.26	0.33	0.29	0.59	0.75	0.65
^{9}Li$(3/2^-_4)$	3.2	0.01	0.04	0.06	0.08	0.21	0.30
^{9}Li$(3/2^-_5)$	4.6	0.000	0.001	0.004	0.000	0.007	0.02
^{6}He$(2^+)+t$ with $[2\otimes 3/2]_{3/2}$							
^{9}Li$(3/2^-_4)$	1.3	0.13	0.15	0.13	0.30	0.33	0.27
^{9}Li$(3/2^-_5)$	2.8	0.06	0.15	0.20	0.33	0.69	0.86
^{6}He$(0^+)+t$ with $[2\otimes 1/2]_{3/2}$							
^{9}Li$(3/2^-_4)$	1.3	0.09	0.10	0.08	0.19	0.21	0.18
^{9}Li$(3/2^-_5)$	2.8	0.09	0.20	0.27	0.44	0.93	1.15
	E_r (MeV)	$\Gamma_{\rm sum}$ (MeV)					
^{10}Be(0^+_3)	3.2	0.19	0.93	1.6			
^{10}Be(0^+_4)	4.7	0.24	0.39	1.0			
^{9}Li$(3/2^-_3)$	1.4	0.59	0.75	0.65			
^{9}Li$(3/2^-_4)$	3.2	0.57	0.75	0.75			
^{9}Li$(3/2^-_5)$	4.6	0.77	1.6	2.0			

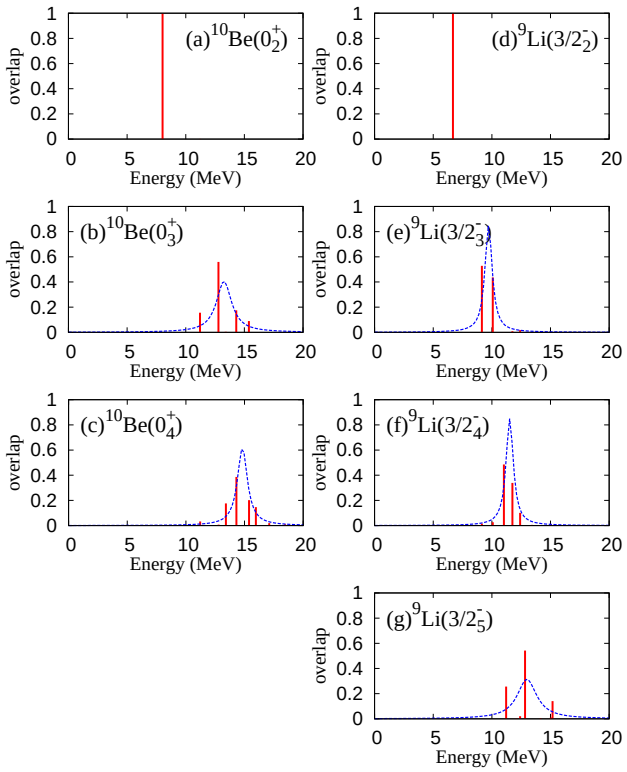

FIG. 3: Distributions of the squared overlap $|\langle\Psi^{J^\pi_k}_{D\leq 8}|\Psi^{J^\pi_l}_{D\leq 15}\rangle|^2$ of the J_k state obtained by the $D \leq 8$ calculation with states obtained by the $D \leq 15$ calculation. Distributions of the $J_k = 0^+_2$, 0^+_3, and 0^+_4 states in ^{10}Be are shown in (a)-(c), and those of the $J_k = 3/2^-_2$, $3/2^-_3$, $3/2^-_4$, and $3/2^-_5$ states in ^{9}Li are shown in (d)-(g). The Breit-Wigner distributions at the energies (E_x) with the widths ($\Gamma_{\rm sum}/2$) for the resonances obtained by the $D \leq 8$ calculation are shown by dashed lines. The largest value of $\Gamma_{\rm sum}$ at $a = 5$, 6, 7 fm table I is adopted for each state.

C. Isoscalar monopole transition strengths

The ISM transition strengths of ^{10}Be(0^+) and ^{9}Li$(3/2^-)$ calculated by the (c+f), $D \leq 8$, and $D \leq 15$ calculations are shown in Figs. 4 and 5. The energy weighted ISM strengths and their Gaussian smeared distributions are shown in Fig. 6. The proton and matter radii, EWSR, EWS, and the ratio EWS/EWSR obtained by three calculations are listed in table II. The experimental radii are also shown in the table. In the (c+f) calculation, the model space is truncated and contains only the configurations (c) and (f), which corresponds to the transverse configurations of ^{6}He with two neutrons in p_x or p_y orbits. In spite of the truncation of ^{6}He configurations, the EWS of the (c+f) result is consistent with those of the $D \leq 8$ and $D \leq 15$ calculations. The reason is that the ground state $|$g.s.$\rangle$ and also its $\mathcal{M}(IS0)$ operated state $\mathcal{M}(IS0)|$g.s.$\rangle$ are contained in the truncated model space of the transverse configurations (c) and (f).

In the (c+f) result of ^{10}Be, the ISM strength is concentrated on the first excited state at $E_x \sim 13$ MeV. In the $D \leq 8$ result, the ISM strengths are split by coupling with other configurations (a), (b), (d), (e). However, the significant strengths remain for the transitions to ^{10}Be(0^+_3) and ^{10}Be(0^+_4) states in the $E_x = 13-15$ MeV. In the $D \leq 15$ result, the strengths are fragmented further because of the coupling with the continuum states, but the strengths are still concentrated in the $E_x = 13-15$ MeV region. In the energy weighted strength distributions shown in Fig. 6(c) , the enhancement of the ISM strengths are found in this energy region. This result indicates that the ISM excitation can be a good probe to observe the ^{6}He$+\alpha$ cluster resonances in ^{10}Be. The ISM strength for the ^{10}Be(0^+_2) is not so remarkable compared with those in the $E_x = 13-15$ MeV region.

In the (c+f) result of ^{9}Li, the ISM strength is some-

what concentrated on the first excited state at $E_x \sim 11$ MeV, but the magnitude of the strength is not so remarkable as the case of ^{10}Be. The strength distributions are fragmented in the $D \leq 8$ result because of the mixing of other configurations (a), (b), (d), (e), and those are strongly scattered in the $D \leq 15$ result because of the coupling with continuum states. The stronger fragmentation of the ISM strengths in ^{9}Li than that in ^{10}Be originates in a variety of angular momentum channels $[I \times J']$ and K-mixing in the total spin-parity $J^\pi = 3/2^-$ of final states. Consequently, there is no concentration of the ISM strengths on the ^{6}He+t cluster resonances in ^{9}Li. Indeed, as shown in Fig. 6(e), the energy weighted strengths are widely distributed and no remarkable strengths to the resonance states in ^{9}Li. The ^{9}Li($3/2^-_2$) has almost no ISM strength, because this state is the band-head state of the $K^\pi = 3/2^-$ band and is not excited by the ISM operator from the ^{9}Li ground state, which has the dominant $K^\pi = 1/2^-$ component.

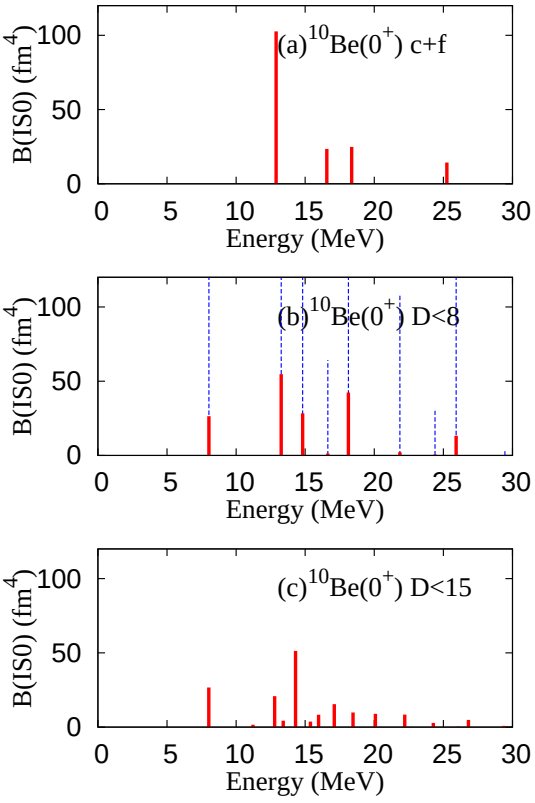

FIG. 4: ISM strength distributions of ^{10}Be(0^+) obtained by the (c+f) , $D \leq 8$, and $D \leq 15$ calculations. Dashed lines in the middle panel (b) for the $D \leq 8$ calculation show fiftyfold values of the strengths.

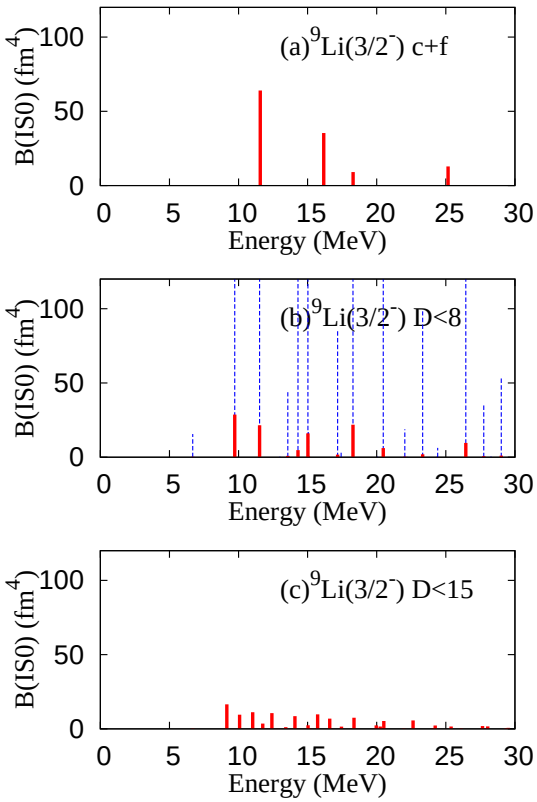

FIG. 5: ISM strength distributions of ^{9}Li($3/2^-$) obtained by the (c+f) , $D \leq 8$, and $D \leq 15$ calculations. Dashed lines in the middle panel (b) for the $D \leq 8$ calculation show fiftyfold values of the strengths.

IV. DISCUSSIONS

In this section, I discuss cluster structures of ^{10}Be(0^+) and ^{9}Li($3/2^-$) in connection with ISM excitations. To analyze cluster structures, I evaluate cluster components at a certain distance by calculating overlaps of the obtained ^{10}Be(0^+) and ^{9}Li($3/2^-$) wave functions with ^{6}He + $\alpha(t)$ wave functions specified by the distance parameter D.

A. Reference ^{6}He(I^+) + $\alpha(t)$ wave functions with D

I consider two types of reference wave functions at a certain distance D. One is the ^{6}He(I^+)+$\alpha(t)$ wave functions with the angular momentum coupling $[I \otimes J']_J$, and the other is the basis wave functions $\Phi_\tau(D)$ used in the GCM calculation. The former is the weak-coupling ^{6}He + $\alpha(t)$ wave functions, in which the internal angular momenta of clusters and the orbital angular momentum of the inter-cluster motion are weakly coupled, whereas the latter is the strong-coupling ^{6}He + $\alpha(t)$ wave functions, in which a deformed ^{6}He cluster is oriented to a

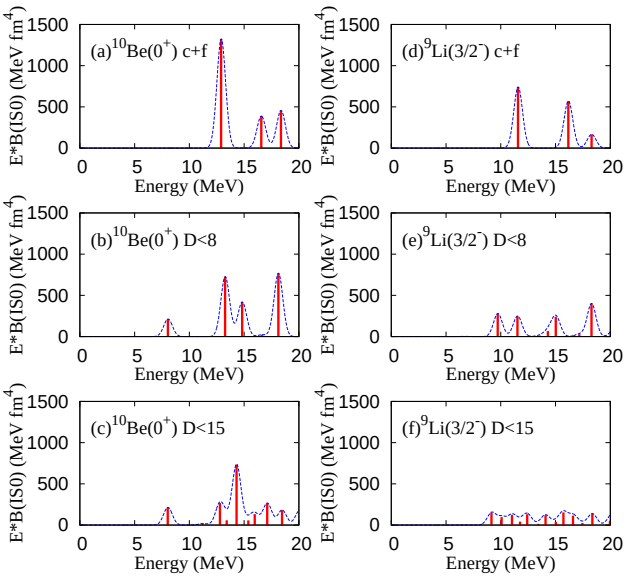

FIG. 6: Energy weighted ISM strengths (solid lines). (a)-(c) The distributions in ^{10}Be(0^+) obtained by the (c+f), $D \leq 8$, $D \leq 15$ calculations, and (d)-(f) the distributions in ^{9}Li($3/2^-$). The Gaussian smeared distributions of the energy weighted ISM strengths with the fixed width $1/\sqrt{\pi}$ are shown by dashed lines.

TABLE II: Theoretical values of proton and matter radii (fm), and the EWSR (MeV fm^4), EWS (MeV fm^4), and the ratio EWS/EWSR of the ISM strengths obtained by the $D \leq 8$ calculation. The experimental proton radii reduced from the charge radii [63, 64], and the experimental matter radii deduced from the interaction cross sections [65] are also shown.

			^{10}Be		
	r_p	r_m	EWSR	EWS	EWS/EWSR
(c+f)	2.31	2.33	4.5×10^2	2.7×10^2	0.60
$D \leq 8$	2.31	2.34	4.5×10^2	2.7×10^2	0.61
$D \leq 15$	2.31	2.34	4.5×10^2	2.7×10^2	0.61
exp.	2.221(18)	2.30(2)			
			^{9}Li		
(c+f)	2.12	2.23	3.7×10^2	1.68×10^2	0.45
$D \leq 8$	2.11	2.22	3.7×10^2	1.68×10^2	0.46
$D \leq 15$	2.11	2.22	3.7×10^2	1.68×10^2	0.46
exp.	2.05(4)	2.32(2)			

specific angle from the $\alpha(t)$ direction.

The ^{6}He(I^+) + $\alpha(t)$ wave functions are constructed by using the ground and the first excite states ^{6}He(0^+) and ^{6}He(2^+) of an isolated ^{6}He cluster described by ho p-shell configurations. The ^{6}He(I^+) + $\alpha(t)$ wave functions with the distance D are given by linear combination of the basis wave functions $P^{J\pi}_{MK}|\Phi_\tau(D)\rangle$ used in the present model, and they are defined as,

$$\Phi^{[I\otimes J']_J}_{^6\mathrm{He}+\alpha(t)}(D) = n_0\mathcal{A}\left\{\phi_{\mathrm{G}}(\boldsymbol{R})\gamma_l(D;r)\left[\varphi^{^6\mathrm{He}}_I\left[\varphi^{\alpha(t)}_{I'}Y_l(\hat{r})\right]_{J'}\right]_J\right\}, \quad (13)$$

$$\gamma_l(D;r) \equiv 4\pi(\frac{2\tilde{\nu}}{\pi})^{\frac{3}{4}} i_l(2\tilde{\nu}Dr)e^{-\tilde{\nu}(r^2+D^2)}, \quad (14)$$

$$\tilde{\nu} \equiv \frac{A_1A_2}{A}\nu, \quad (15)$$

$$\phi_{\mathrm{G}}(\boldsymbol{R}) = \left(\frac{2A\nu}{\pi}\right)e^{-A\nu\boldsymbol{R}^2}, \quad (16)$$

where i_l is the modified spherical Bessel function, $\varphi^{^6\mathrm{He}}_I$ and $\varphi^{\alpha(t)}_{I'}$ are the internal wave functions of ^{6}He(I^+) and $\alpha(t)$ clusters with the internal angular momentum I and I', respectively. ϕ_{G} is the wave function of the center of mass motion and n_0 is the normalization factor.

For the strong-coupling ^{6}He + $\alpha(t)$ wave functions, I consider the J^π and K projected states of the basis wave functions $\Phi_\tau(D)$ with specific configurations as,

$$\Phi^{(T)}_{^6\mathrm{He}+\alpha(t)}(D) \equiv n_0P^{J\pi}_{M0(1/2)}|\Phi_{\tau=f}(D)\rangle, \quad (17)$$

$$\Phi^{(A)}_{^6\mathrm{He}+\alpha(t)}(D) \equiv n_0P^{J\pi}_{M0(1/2)}|\Phi_{\tau=a}(D)\rangle, \quad (18)$$

$$\Phi^{(I_z2)}_{^6\mathrm{He}+t}(D) \equiv n_0P^{J\pi}_{M,-3/2}|\Phi_{\tau=c}(D)\rangle. \quad (19)$$

$\Phi^{(T)}_{^6\mathrm{He}+\alpha(t)}(D)$ is the jj coupling transverse (T) configuration corresponding to the configuration (f) with two neutrons in the transverse orbits with $|j_z| = 3/2$, whereas $\Phi^{(A)}_{^6\mathrm{He}+\alpha(t)}(D)$ is the ls coupling aligned (A) configuration given by the configuration (a) with two neutrons coupling to $S = 0$ in the aligned orbit p_z. In a short distance (D) region, configurations other than transverse configurations feel strong Pauli blocking, and therefore, $\Phi^{(T)}_{^6\mathrm{He}+\alpha(t)}(D)$ is most favored. Indeed, the ground state wave function has the largest overlap with $\Phi^{(T)}_{^6\mathrm{He}+\alpha(t)}(D)$ with $D = 2-3$ fm as shown later. The configuration (a), i.e., $\Phi^{(A)}_{^6\mathrm{He}+\alpha(t)}(D)$ corresponds to the molecular σ-orbital structure, and this component with $D = 4-5$ fm has a large overlap with the ^{10}Be(0^+_2). $\Phi^{(I_z2)}_{^6\mathrm{He}+t}(D)$ is the $K = -3/2$ state projected from the ls coupling transverse configuration given by the configuration (c), in which a $S = 0$ two-neutron pair in the ^{6}He cluster is rotating to give $I_z = -2$. $\Phi^{(I_z2)}_{^6\mathrm{He}+t}(D)$ with $D = 2-3$ fm is the dominant component of the ^{9}Li($3/2^-_2$).

Thus defined weak-coupling and strong-coupling reference wave functions, $\Phi^{[I\otimes J']_J}_{^6\mathrm{He}+\alpha(t)}(D)$ and $\Phi^{(T,A,I_z2)}_{^6\mathrm{He}+\alpha(t)}(D)$, are not orthogonal to each other. In Fig. 7, I show squared overlaps of $\Phi^{[I\otimes J']_J}_{^6\mathrm{He}+\alpha(t)}(D)$ with $\Phi^{(T,A,I_z2)}_{^6\mathrm{He}+\alpha(t)}(D)$. In a short distance region, only transverse configurations are Pauli allowed but other configurations feel strong Pauli blocking because of the antisymmetrization effect between clusters. As a result, both of the ^{6}He(0^+)+α and

^{6}He$(2^+)+\alpha$ wave functions, $\Phi^{[0\otimes 0]_0}_{^6\mathrm{He}+\alpha}(D)$ and $\Phi^{[2\otimes 2]_0}_{^6\mathrm{He}+\alpha}(D)$, have dominant overlaps with the transverse configuration $\Phi^{(T)}_{^6\mathrm{He}+\alpha}(D)$ but no overlap with the aligned configuration $\Phi^{(A)}_{^6\mathrm{He}+\alpha}(D)$. This means that the ^{6}He$(0^+)+\alpha$ and ^{6}He$(2^+)+\alpha$ wave functions at the short distance are almost equivalent to the $\Phi^{(T)}_{^6\mathrm{He}+\alpha}(D)$ and contain no $\Phi^{(A)}_{^6\mathrm{He}+\alpha}(D)$ component. As for the ^{6}He$+t$ wave functions at a short distance D, the ^{6}He$(0^+)+t$ wave function is almost equivalent to $\Phi^{(T)}_{^6\mathrm{He}+t}(D)$, the ^{6}He$(2^+)+t$ wave function is a mixing of $\Phi^{(T)}_{^6\mathrm{He}+t}(D)$ and $\Phi^{(I_z 3/2)}_{^6\mathrm{He}+t}(D)$, whereas they contain no $\Phi^{(A)}_{^6\mathrm{He}+t}(D)$ component. This is a trivial consequence of the antisymmetrization of the ^{6}He$+\alpha$ cluster wave functions, and it indicates that, at a short distance, the weak-coupling ^{6}He$+\alpha(t)$ wave functions have less physical meaning than the strong-coupling ^{6}He$+\alpha(t)$ wave functions. In an enough large distance D region free from the Pauli blocking between two clusters, $\Phi^{[I\otimes J']_J}_{^6\mathrm{He}+\alpha(t)}(D)$ with different I and J' is orthogonal to each other, and has overlaps with $\Phi^{(T,A,I_z 2)}_{^6\mathrm{He}+\alpha(t)}(D)$ in specific ratios.

B. Cluster structures of ^{10}Be(0^+) and ^{9}Li$(3/2^-)$

To analyze cluster structures of the obtained ^{10}Be(0^+) and ^{9}Li$(3/2^-)$, I calculate the overlaps with the reference ^{6}He$+\alpha(t)$ wave functions at the distance D, $\Phi^{[I\otimes J']_J}_{^6\mathrm{He}+\alpha(t)}(D)$ and $\Phi^{(T,A,I_z 2)}_{^6\mathrm{He}+\alpha(t)}(D)$. Figures 8 and 9 show the squared overlaps of the ^{10}Be(0^+) and ^{9}Li$(3/2^-)$ obtained by the $D\leq 8$ calculation with the ^{6}He$+\alpha(t)$ wave functions plotted as functions of D.

The ^{10}Be ground state has the dominant overlap with the transverse configuration $\Phi^{(T)}_{^6\mathrm{He}+\alpha}(D)$ at $D\sim 3$ fm and almost no overlap with the aligned configuration $\Phi^{(A)}_{^6\mathrm{He}+\alpha}(D)$. The ^{10}Be$(0^+_2)$ is dominated by $\Phi^{(A)}_{^6\mathrm{He}+\alpha}(D)$ at $D=4-5$ fm. This is consistent with the molecular σ-orbital structure of the ^{10}Be(0^+_2) as discussed in the preceding works. Thus, the low-lying states, ^{10}Be(0^+_1) and ^{10}Be(0^+_2), can be clearly classified by the strong-coupling ^{6}He$+\alpha$ wave functions, meaning that these states have strong-coupling cluster structures rather than weak-coupling ones. In this strong-coupling cluster picture, the excitation from the ^{10}Be(0^+_1) to the ^{10}Be(0^+_2) is understood by the rotation of the deformed ^{6}He-cluster from the transverse configuration to the aligned configuration with some extent of spatial development of clustering. Because of the difference in the ^{6}He-cluster orientation, i.e., the difference in two-neutron configurations, the ISM transition is suppressed for the transition between ^{10}Be(0^+_1) and ^{10}Be(0^+_2) even though the ^{10}Be(0^+_2) has the developed cluster structure.

The ^{6}He$+\alpha$ resonance states, ^{10}Be(0^+_3) and ^{10}Be(0^+_4), have spatially developed cluster structures with significant cluster components at $D=6-7$ fm. These states

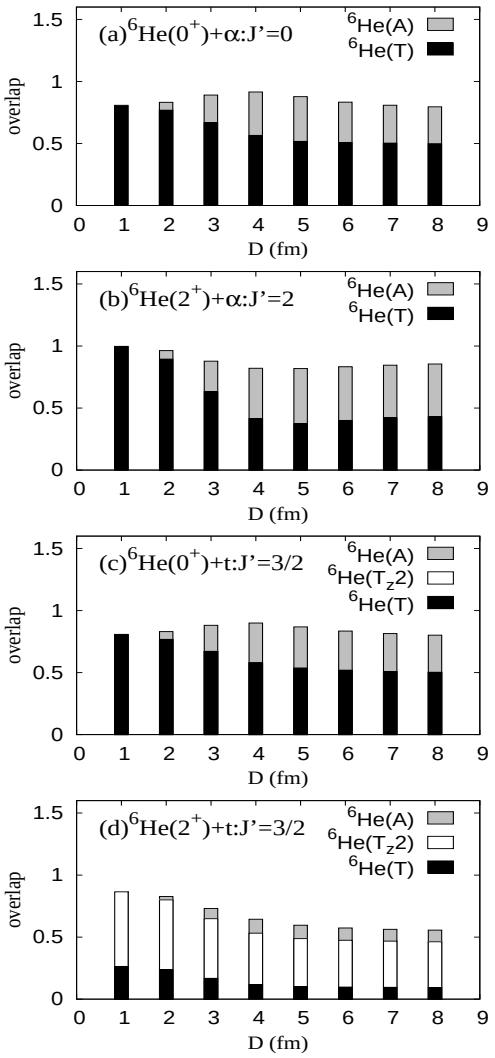

FIG. 7: Squared overlaps between the weak-coupling cluster wave functions $\Phi^{[I\otimes J']_J}_{^6\mathrm{He}+\alpha(t)}(D)$ and the strong-coupling cluster wave functions $\Phi^{(T,A,I_z 2)}_{^6\mathrm{He}+\alpha(t)}(D)$. The squared overlaps of (a) $\Phi^{[0\otimes 0]_0}_{^6\mathrm{He}+\alpha}(D)$, (b) $\Phi^{[2\otimes 2]_0}_{^6\mathrm{He}+\alpha}(D)$, (c) $\Phi^{[0\otimes 3/2]_{3/2}}_{^6\mathrm{He}+t}(D)$, and (d) $\Phi^{[0\otimes 3/2]_{3/2}}_{^6\mathrm{He}+t}(D)$ with $\Phi^{(T,A,I_z 2)}_{^6\mathrm{He}+\alpha(t)}(D)$ are shown.

show intermediate features of strong-coupling and weak-coupling cluster structures. The ^{10}Be(0^+_3) state has the dominant component of $\Phi^{(T)}_{^6\mathrm{He}+\alpha}(D)$ at $D=6-7$ fm and is interpreted as a higher nodal state excited from the ground state in the model space of the transverse configuration (f). It has the significant ^{6}He$(0^+)+\alpha$ component and can be also regarded as a ^{6}He$(0^+)+\alpha$ resonance. The ^{10}Be(0^+_4) has the relatively larger ^{6}He$(2^+)+\alpha$ component at $D=6-7$ fm and is regarded as a ^{6}He$(2^+)+\alpha$ resonance.

Also in ^{9}Li, the bound states, ^{9}Li$(3/2^-_1)$ and ^{9}Li$(3/2^-_2)$, can be clearly classified by the strong-coupling ^{6}He$+t$ wave functions. The ^{9}Li ground state has the

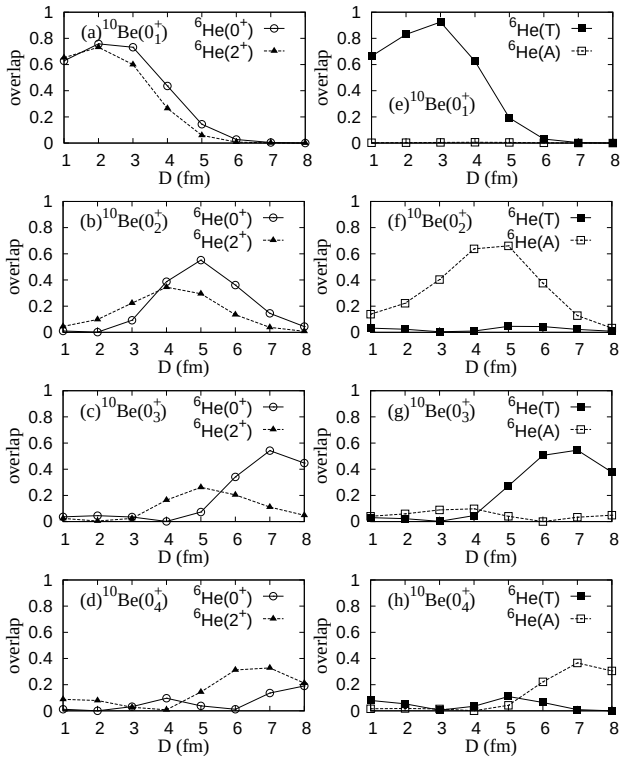

FIG. 8: ^{6}He + α components in ^{10}Be(0^+) obtained by the $D \leq 8$ calculation. (a-d) Squared overlaps of ^{10}Be(0^+) with $\Phi^{[0\otimes0]_0}_{^6\mathrm{He}+\alpha}(D)$ and $\Phi^{[2\otimes2]_0}_{^6\mathrm{He}+\alpha}(D)$. (e-h) Squared overlaps of ^{10}Be(0^+) with $\Phi^{(T)}_{^6\mathrm{He}+\alpha}(D)$ and $\Phi^{(A)}_{^6\mathrm{He}+\alpha}(D)$.

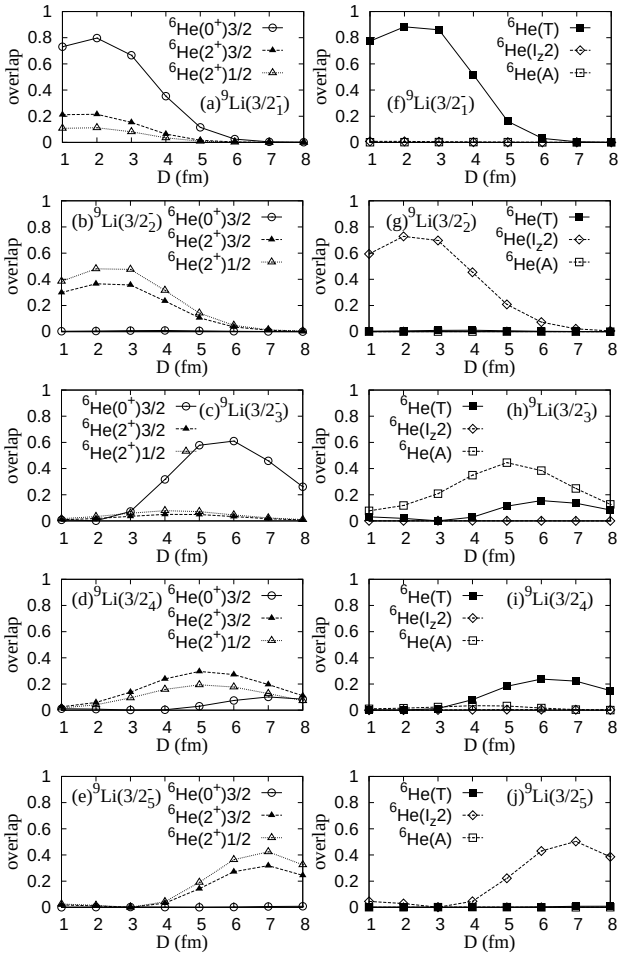

FIG. 9: ^{6}He + t components in ^{9}Li($3/2^-$) obtained by the $D \leq 8$ calculation. (a-e) Squared overlaps of ^{9}Li($3/2^-$) with $\Phi^{[0\otimes3/2]_{3/2}}_{^6\mathrm{He}+t}(D)$, $\Phi^{[2\otimes3/2]_{3/2}}_{^6\mathrm{He}+t}(D)$, and $\Phi^{[2\otimes1/2]_{3/2}}_{^6\mathrm{He}+t}(D)$. (f-j) Squared overlaps of the ^{9}Li($3/2^-$) with $\Phi^{(T)}_{^6\mathrm{He}+t}(D)$, $\Phi^{(A)}_{^6\mathrm{He}+t}(D)$, and $\Phi^{(I_z2)}_{^6\mathrm{He}+t}(D)$.

dominant overlap with $\Phi^{(T)}_{^6\mathrm{He}+t}(D)$ at $D = 2-3$ fm and almost no overlap with $\Phi^{(A)}_{^6\mathrm{He}+\alpha}(D)$, which is suppressed by the Pauli blocking effect at the short distance. The ^{9}Li($3/2^-_2$) is dominated by $\Phi^{(I_z2)}_{^6\mathrm{He}+t}(D)$ at $D \sim 2$ fm and can be regarded as the $K = 3/2$ state. The resonance states of ^{9}Li($3/2^-$) have significant cluster components in the $D = 5-7$ fm meaning the spatially developed ^{6}He$+t$ clustering. The ^{9}Li($3/2^-_3$) has the remarkable ^{6}He(0^+)$+t$ component and relatively small ^{6}He(2^+) $+ t$ component, and therefore is regarded as a weak-coupling ^{6}He(0^+) $+ t$ cluster resonance. The ^{9}Li($3/2^-_4$) and ^{9}Li($3/2^-_5$) can be regarded as ^{6}He(2^+) $+ t$ cluster resonances because they have significant ^{6}He(2^+) $+ t$ components and relatively small ^{6}He(0^+) $+ t$ components.

The appearance of the weak-coupling ^{6}He(0^+)$+t$ cluster resonance in the ^{9}Li($3/2^-_3$) is a specific feature of the ^{9}Li system different from the ^{10}Be system, in which each ^{6}He + α cluster resonance is not a pure weak-coupling ^{6}He(I^+) + α state. One of the keys for this difference between ^{9}Li and ^{10}Be is the presence or absence of the molecular σ-orbital structure below the threshold energy. In ^{10}Be, the molecular σ-orbital structure is favored and it appears in the ^{10}Be(0^+_2). Note that the molecular σ-orbital structure corresponds to the ^{6}He(A) + α wave function in the present model. It is important that the orthogonal condition of the ^{10}Be(0^+_2) to the ground state is satisfied by the orthogonality of the orientation of the deformed ^{6}He cluster. In higher states, the ^{6}He + α clustering develops keeping the orthogonal condition to the lower states, ^{10}Be(0^+_1) and ^{10}Be(0^+_2). The existence of the ^{10}Be(0^+_2) having the aligned configuration ^{6}He(A)+α at the moderate distance ($D = 4-5$ fm) somewhat suppresses the weak-coupling feature of ^{6}He + α cluster resonances because the orthogonal condition to the ^{10}Be(0^+_2) depends on the orientation of the deformed ^{6}He-cluster. In contrast, the molecular σ-orbital structure is not favored in ^{9}Li because of the asymmetry of the $\alpha + t$ core. In the developed cluster states, the rotational symmetry of the subsystem ^{6}He is restored in the absence of the molecular σ-orbital structure, and the weak-coupling ^{6}He + t clustering is favored to form the ^{6}He(0^+) + t

cluster resonance in the ^{9}Li($3/2^-_3$).

The ^{6}He(0^+)+α and ^{6}He(2^+)+α components at $D = 5$ fm and $D = 7$ fm in ^{10}Be are shown in Fig. 10. The figure shows the squared overlaps of $\Phi^{[I\otimes J']_J}_{^6\mathrm{He}+\alpha}(D)$ with the ^{10}Be(0^+) obtained by the $D \le 8$ and $D \le 15$ calculations. At $D = 5$ fm, the ^{6}He(0^+) + α component is concentrated at 8 MeV for the ^{10}Be(0^+_2), which has also the significant ^{6}He(2^+) + α component showing the development of the strong-coupling cluster structure (Fig. 10(a)-(d)). At $D = 7$ fm, the ^{6}He(0^+) + α component is concentrate on the ^{10}Be(0^+_3) at 13 MeV, whereas the ^{6}He(2^+) + α component is significant in the ^{10}Be(0^+_4) at 15 MeV in the $D \le 8$ calculation (Fig. 10(e) and (f)). Also in the $D \le 15$ calculations, the concentration of the ^{6}He(0^+) + α component around 13 MeV and that of the ^{6}He(2^+) + α component around 15 MeV can be seen though the components are somewhat fragmented (Fig. 10(g) and (h)).

Figure 11 shows ^{6}He(0^+) + t and ^{6}He(2^+) + t components at $D = 5$ fm and $D = 7$ fm in ^{9}Li. The distributions of the components are qualitatively similar at $D = 5$ fm and $D = 7$ fm. The ^{6}He(0^+) + t component is concentrated at 10 MeV for the ^{9}Li($3/2^-_3$) in the $D \le 8$ calculation (Fig. 11(a) and (e)). Even in the $D \le 15$ calculation, the significant ^{6}He(0^+) + t component is found in the corresponding energy region around 9 MeV (Fig. 11(c) and (g)). The ^{6}He(2^+) + t component is significantly contained in states in the 11 − 14 MeV region.

It should be point out that the distributions of the ^{6}He(0^+) + α and ^{6}He(0^+) + t components shown in Figs. 10 and 11 are not necessarily consistent with the ISM strength distributions shown in Figs. 4 and 5. In particular, in spite of the remarkable ^{6}He(0^+) + t component in the ^{9}Li($3/2^-$) state around 10 MeV, there is no significant ISM strength in the corresponding energy region. Also for ^{10}Be(0^+), even though the ^{10}Be(0^+_2) has the remarkable ^{6}He(0^+) + α component, the ISM transition to this state is relatively suppressed compared with other states. As discussed later, there is no one to one correspondence between the ISM excitation and the ^{6}He(0^+) + α component, but the ISM operator more directly excites the specific type of strong-coupling cluster structures embedded in the ground state.

C. Isoscalar monopole excitations in cluster structures

Enhancement of ISM transitions to cluster states has been discussed for stable nuclei and also unstable nuclei [26, 59–61]. As discussed by Yamada *et al.*, ISM strengths are enhanced for transitions from the ground state to cluster excited states because the ISM operator $\mathcal{M}(IS0)$ excites the inter-cluster motion through the r^2 term in $\mathcal{M}(IS0)$ [61]. As shown in Ref. [61], $\mathcal{M}(IS0)$

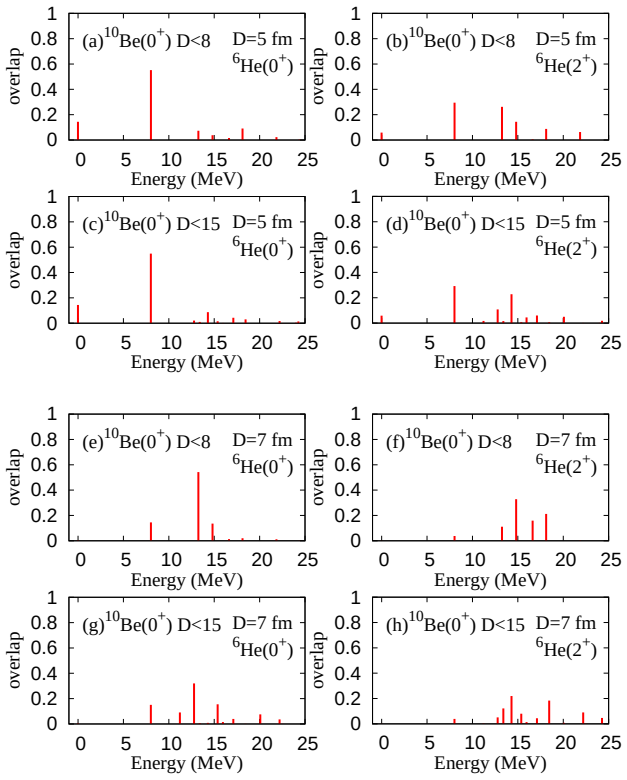
(a)10Be(0+) D<8 D=5 fm 6He(0+)
(b)10Be(0+) D<8 D=5 fm 6He(2+)
(c)10Be(0+) D<15 D=5 fm 6He(0+)
(d)10Be(0+) D<15 D=5 fm 6He(2+)
(e)10Be(0+) D<8 D=7 fm 6He(0+)
(f)10Be(0+) D<8 D=7 fm 6He(2+)
(g)10Be(0+) D<15 D=7 fm 6He(0+)
(h)10Be(0+) D<15 D=7 fm 6He(2+)
overlap
Energy (MeV)

FIG. 10: Distributions of ^{6}He(0^+) + α and ^{6}He(2^+) + α components in ^{10}Be(0^+). (a)(b) Squared overlaps of ^{10}Be(0^+) obtained by the $D \le 8$ calculation with $\Phi^{[0\otimes 0]_0}_{^6\mathrm{He}+\alpha}(D)$ and $\Phi^{[2\otimes 2]_0}_{^6\mathrm{He}+\alpha}(D)$ at $D = 5$ fm, and (e)(f) those at $D = 7$ fm. (c)(d)(g)(h) Same but for the $D \le 15$ calculation.

can be rewritten as

$$\mathcal{M}(IS0) = \frac{A_1 A_2}{A} r^2 + \sum_{i\in C} (\boldsymbol{r}_i - \boldsymbol{R}_1)^2 + \sum_{i\in C'} (\boldsymbol{r}_i - \boldsymbol{R}_2)^2 , \tag{20}$$

where $\boldsymbol{R}_1$ and $\boldsymbol{R}_2$ is the center of mass coordinates of the first (C) and second (C') clusters. If the antisymmetrization is ignored, the first term excites the inter-cluster motion whereas the second and third terms cause the ISM excitations of C and C' clusters.

In the ISM excitations, the $\mathcal{M}(IS0)$ operated state, $\mathcal{M}(IS0)|\mathrm{g.s.}\rangle$ is regarded as the door-way state that is initially produced by the ISM excitation. Provided that excitations of the inter-cluster motion (cluster mode) are decoupled well from internal excitations of the clusters, the ISM strengths to cluster states are nothing but distributions of the door-way state $\mathcal{M}(IS0)|\mathrm{g.s.}\rangle$ projected onto the cluster model space, $\hat{P}(C + C')\mathcal{M}(IS0)|\mathrm{g.s.}\rangle$, which approximately corresponds to the door-way state excited from the ground state by the r^2 operator. Here $\hat{P}(C + C')$ is the projection operator onto the $C + C'$ cluster model space. In the present case, ISM strengths indicate the distributions of the projected door-way state $\hat{P}(^6\mathrm{He} + \alpha(t))\mathcal{M}(IS0)|\mathrm{g.s.}\rangle$ in the ^{6}He + $\alpha(t)$ cluster

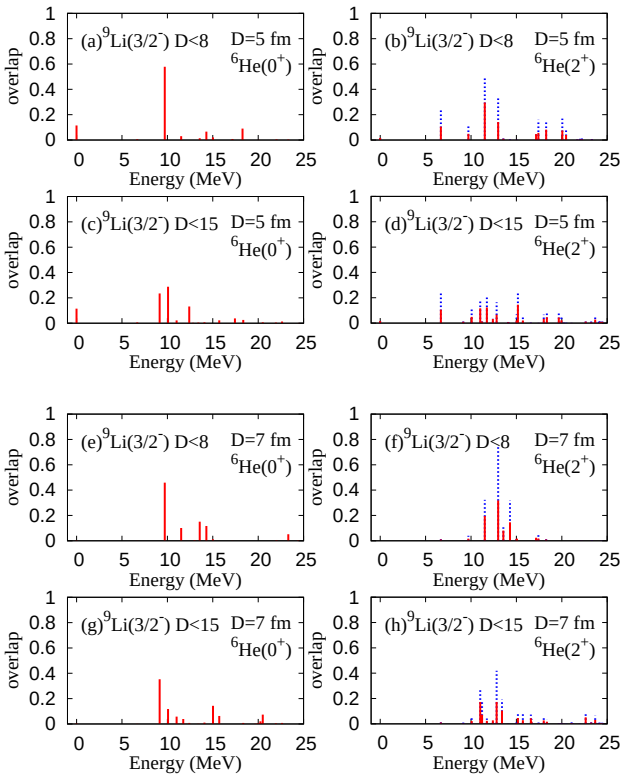
(a)^{9}Li(3/2$^-$) D<8 D=5 fm ^{6}He(0$^+$)
(b)^{9}Li(3/2$^-$) D<8 D=5 fm ^{6}He(2$^+$)
(c)^{9}Li(3/2$^-$) D<15 D=5 fm ^{6}He(0$^+$)
(d)^{9}Li(3/2$^-$) D<15 D=5 fm ^{6}He(2$^+$)
(e)^{9}Li(3/2$^-$) D<8 D=7 fm ^{6}He(0$^+$)
(f)^{9}Li(3/2$^-$) D<8 D=7 fm ^{6}He(2$^+$)
(g)^{9}Li(3/2$^-$) D<15 D=7 fm ^{6}He(0$^+$)
(h)^{9}Li(3/2$^-$) D<15 D=7 fm ^{6}He(2$^+$)
overlap
Energy (MeV)

FIG. 11: Distributions of ^{6}He$(0^+)+t$ and ^{6}He$(2^+)+t$ components in ^{9}Li$(3/2^-)$. (a)(b) Squared overlaps of ^{9}Li$(3/2^-)$ obtained by the $D\le 8$ calculation with $\Phi^{[0\otimes 3/2]_{3/2}}_{^6\mathrm{He}+t}(D)$ (solid lines), $\Phi^{[2\otimes 3/2]_{3/2}}_{^6\mathrm{He}+t}(D)$ (solid lines), and $\Phi^{[2\otimes 1/2]_{3/2}}_{^6\mathrm{He}+t}(D)$ (dashed lines) at $D=5$. (e)(f) Those at $D=7$ fm. (c)(d)(g)(h) Same but for the $D\le 15$ calculation.

model space.

As discussed previously, the low-lying states of ^{10}Be and ^{9}Li are understood by strong-coupling cluster structures. In particular, the ground state is dominated by the transverse configuration $\Phi^{(T)}_{^6\mathrm{He}+\alpha(t)}(D)$ with the distance $D=2-3$ fm. Therefore, the projected door-way state $P(^6\mathrm{He}+\alpha(t))\mathcal{M}(IS0)|\mathrm{g.s.}\rangle$ is approximately included by the subspace with the specific configuration $\Phi^{(T)}_{^6\mathrm{He}+\alpha(t)}(D)$ because the ISM operator excites the inter-cluster motion through the r^2 term but does not change the orientation of the deformed ^{6}He cluster. Figure 12 shows the ISM strengths for transition from the ^{10}Be and ^{9}Li ground state to specific configurations. One is the transverse configuration $\Phi^{(T)}_{^6\mathrm{He}+\alpha(t)}(D)$ and the other is the aligned configuration $\Phi^{(A)}_{^6\mathrm{He}+\alpha(t)}(D)$. The strengths of the ISM transitions from the ground state is calculated as

$$B(IS0;\mathrm{g.s.}\to\Phi^{(T,A)}_{^6\mathrm{He}+\alpha(t)}(D))$$
$$=\frac{1}{2J+1}\left|\left\langle \mathrm{g.s.}||\mathcal{M}(IS0)||\Lambda_{\mathrm{g.s.}}\Phi^{(T,A)}_{^6\mathrm{He}+\alpha(t)}(D)\right\rangle\right|^2 \quad (21)$$
$$\Lambda_{\mathrm{g.s.}}\equiv 1-|\mathrm{g.s.}\rangle\langle\mathrm{g.s.}|, \quad (22)$$

where the normalizations of the initial and final states are chosen to be one, and the orthogonal condition of the final state to the initial state is satisfied by the projection operator $\Lambda_{\mathrm{g.s.}}$. As seen in the figure, the calculated ISM strengths show remarkable transitions to $\Phi^{(T)}_{^6\mathrm{He}+\alpha(t)}(D)$ at $D=4-5$ fm but almost no transition to $\Phi^{(A)}_{^6\mathrm{He}+\alpha(t)}(D)$ as expected from the dominant $\Phi^{(T)}_{^6\mathrm{He}+\alpha(t)}(D)$ component in the initial state $|\mathrm{g.s.}\rangle$. It means that the door-way state excited from the ground state by the ISM operator dominantly contains the transverse configuration of the ^{6}He cluster.

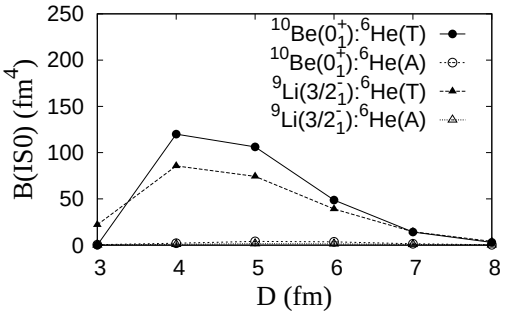

FIG. 12: ISM strengths $B(IS0;\mathrm{g.s.}\to\Phi^{(T,A)}_{^6\mathrm{He}+\alpha(t)}(D))$ for the transitions from the ^{10}Be and ^{9}Li ground states obtained by the $D\le 8$ calculation to $\Phi^{(T,A)}_{^6\mathrm{He}+\alpha(t)}(D)$. $B(IS0;\mathrm{g.s.}\to\Phi^{(T,A)}_{^6\mathrm{He}+\alpha(t)}(D))$ is defined in (21).

Let us discuss again the IMS strengths obtained by three calculations, (c+f), $D\le 8$, and $D\le 15$. As already shown in Table II, the EWS obtained by the (c+f) calculation is almost consistent with that obtained by the $D\le 8$ calculation with full ^{6}He configurations. It meant that the door-way state directly produced from the ground state with the ISM operator are mostly contained in the truncated model space of the configurations (c) and (f). As shown in Figs. 4(a) and 5(a), the ISM strengths are concentrated in a few low-lying states in the the (c+f) calculation meaning that the door-way state is distributed in these few states of the truncated model space. However, in the $D\le 8$ calculation with full configurations of $^6\mathrm{He}+\alpha(t)$, the ISM strengths are somewhat fragmented through coupling of the configuration $\Phi^{(T)}_{^6\mathrm{He}+\alpha(t)}(D)$ with other configurations. The ISM strengths should reflect the distributions of the $\Phi^{(T)}_{^6\mathrm{He}+\alpha}(D)$ and $\Phi^{(T)}_{^6\mathrm{He}+t}(D)$ components in the obtained ^{10}Be(0^+) and ^{9}Li$(3/2^-)$. As already shown in Fig. 12, the $\Phi^{(T)}_{^6\mathrm{He}+\alpha(t)}(D)$ configuration has the strong ISM transition in the $D=4-5$ fm region meaning that the door-way state excited from the ground state by the ISM operator has large overlap with this state. In Figs. 13 and 14, I show the squared overlaps of ^{10}Be(0^+) and ^{9}Li$(3/2^-)$ obtained by three calculations

with $\Phi^{(T)}_{^6\mathrm{He}+\alpha}(D)$ and $\Phi^{(T)}_{^6\mathrm{He}+t}(D)$ at $D = 5$ fm. For comparison, I also show the components of the aligned configuration $\Phi^{(A)}_{^6\mathrm{He}+\alpha(t)}(D)$ at $D = 5$ fm. Comparing the results of Figs. 4 and 5 and those of Figs. 13 and 14, the ISM strength distributions can be qualitatively described by the distributions of the $\Phi^{(T)}_{^6\mathrm{He}+\alpha(t)}(D)$ component. In the $D \leq 15$ calculation of ^{9}Li, the fragmentation of the ISM strengths for the $^6\mathrm{He} + t$ cluster resonances around 10 MeV is understood by the strong fragmentation of the $\Phi^{(T)}_{^6\mathrm{He}+\alpha(t)}(D)$ component because of the coupling with other configurations.

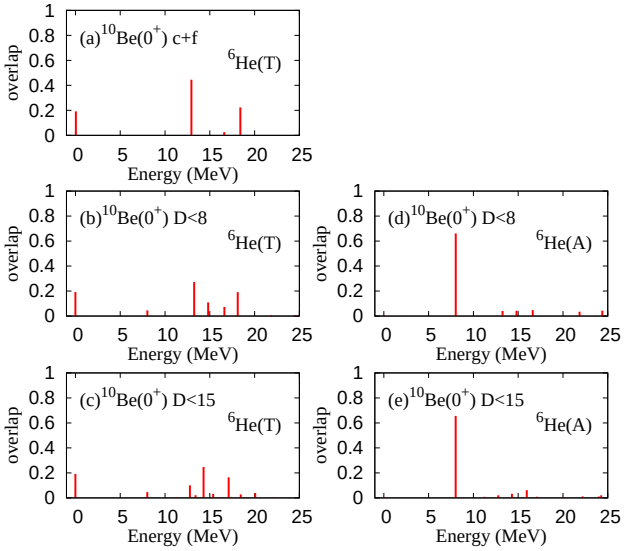

FIG. 13: Distributions of squared overlaps of $\Phi^{(T,A)}_{^6\mathrm{He}+\alpha}(D)$ at $D = 5$ fm with the ^{10}Be(0$^+$) obtained by the (c+f), $D \leq 8$, and $D \leq 15$ calculations.

Let us give more general discussions of the door-way state excited from the ground state to cluster states by the ISM operator. As mentioned previously, the projected door-way state approximately corresponds to the r^2 operated state of the ground state. In case that the ground state contains a deformed cluster with a specific orientation, the inter-cluster motion is excited from the ground state to the door-way state keeping the orientation of the cluster as it is in the ground state because the r^2 operator does not bring rotation of clusters. Schematic figures are shown in Fig. 15. When the system consists of two spin-less clusters such as $^{16}\mathrm{O} + \alpha$, in which both clusters are ls-closed shell nuclei, the projected door-way state can be concentrated on a $^{16}\mathrm{O}+\alpha$ cluster state, and therefore, the ISM transition should be strong for the $^{16}\mathrm{O} + \alpha$ cluster state (see Fig. 15(a)). However, in the cases of $^6\mathrm{He} + \alpha$ and $^6\mathrm{He} + t$ cluster states in ^{10}Be and ^{9}Li, the ^{6}He cluster is not a ls-closed shell nucleus but is deformed in the ^{10}Be and ^{9}Li ground states because of the Pauli blocking effect between clusters (see Fig. 15(b) and (c)). The deformed ^{6}He cluster is the mixed state of

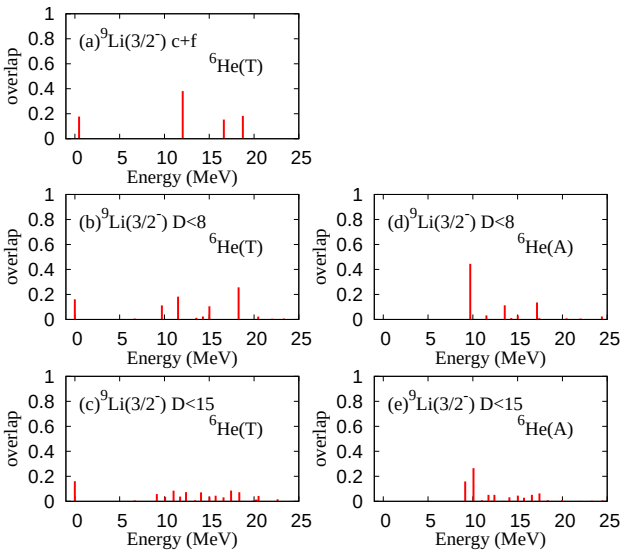

FIG. 14: Distributions of squared overlaps of $\Phi^{(T,A)}_{^6\mathrm{He}+t}(D)$ at $D = 5$ fm with the $^9\mathrm{Li}(3/2^-)$ obtained by the (c+f), $D \leq 8$, and $D \leq 15$ calculations.

different spin states, $^6\mathrm{He}(I)$. In the asymptotic region of a large inter-cluster distance, the deformed cluster is not favored but the angular-momentum eigen states $^6\mathrm{He}(I)$ are favored because of the restoration of the rotational symmetry of the subsystem. Moreover, in the $^6\mathrm{He} + t$ system, the second cluster (t) has the finite intrinsic spin $I' = 1/2$. Therefore, the projected door-way state is fragmented in $^6\mathrm{He} + t$ cluster states through the coupling of the angular momenta I and I' of the clusters and the orbital angular momentum of the inter-cluster motion. As a result, the ISM strengths can be strongly fragmented. In the $^6\mathrm{He} + \alpha$ system, since the angular momentum coupling is not so strong for the spin-less α cluster, the fragmentation of the door-way state can be weaker than the $^6\mathrm{He}+t$ system. Therefore, the fragmentation of the ISM strengths to $^6\mathrm{He} + \alpha$ cluster states is not so strong as that to $^6\mathrm{He} + t$ cluster states.

V. SUMMARY

The ISM transitions from the ground states to cluster states in ^{10}Be and ^{9}Li were investigated with the $^6\mathrm{He}+\alpha$ and $^6\mathrm{He} + t$ cluster models, respectively. In the calculation, the resonance states were obtained in a bound state approximation. The $^6\mathrm{He} + \alpha$ and $^6\mathrm{He} + t$ widths of the resonances were estimated by the method using the reduced width amplitudes obtained by the calculation with $D \leq 8$ fm. The coupling with continuum states evaluated by changing the boundary size from $D \leq 8$ fm to $D \leq 15$ fm shows consistent results with the decay widths estimated by the bound state approximation with $D \leq 8$ fm.

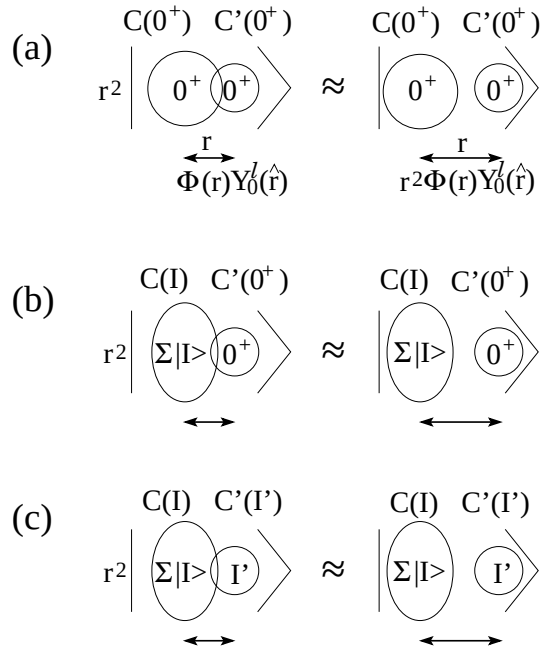

FIG. 15: Schematic figures for ISM excitations to cluster states. (a) A system of two clusters that are spin-less ls-closed shell nuclei. (b) A system of a deformed cluster and a spin-less ls-closed cluster. (b) A system of a deformed cluster and a finite-spin cluster.

In ^{10}Be, the $^6\mathrm{He}+\alpha$ cluster resonances were obtained as the $^{10}\mathrm{Be}(0^+_3)$ and $^{10}\mathrm{Be}(0^+_4)$ above the ^{6}He+α threshold energy. The significant ISM strengths were obtained for the transitions to these resonances. In ^{9}Li, the $^6\mathrm{He}+t$ cluster resonances were obtained as the $^9\mathrm{Li}(3/2^-_{3,4,5})$ above the $^6\mathrm{He}+t$ threshold energy. The ISM strengths are strongly fragmented and show no enhancement for these ^{6}He+t cluster resonances differently from the ^{6}He+α cluster resonances in ^{10}Be.

By analyzing the cluster components of excited states, the relation of the ISM excitations with the cluster components were discussed. It was found that the ISM strength distributions do not directly correspond to the distributions of the $^6\mathrm{He}(0^+)+\alpha$ and $^6\mathrm{He}(0+)+t$ components but they are distributed via components of the deformed ^{6}He cluster configuration with a specific orientation. The ISM strengths to cluster states are the distributions of the door-way state, which is excited from the ground state by the r^2 operator, in the cluster model space. Since the ^{10}Be and ^{9}Li ground states are dominated by the the transverse configuration of the deformed ^{6}He cluster, the door-way state also dominantly contains the transverse configuration because the ISM operator excites the inter-cluster motion through the r^2 term but does not change the orientation of the deformed ^{6}He cluster. The door-way state distributions, which is originally concentrated on the specific configuration, are fragmented in final states in the full model space because of mixing with other configurations as well as the angular momentum coupling. This is an interpretation of the fragmentation of the ISM strengths in ^{10}Be and ^{9}Li. It should be stressed that the ISM excitations more directly reflect the strong-coupling cluster features which is originally embedded in the ground state rather than the weak-coupling cluster features.

Acknowledgments

The author would like to thank Dr. Kimura and Dr. Suhara for fruitful discussions. The computational calculations of this work were performed by using the supercomputer in the Yukawa Institute for theoretical physics, Kyoto University. This work was supported by JSPS KAKENHI Grant Number 26400270.

Appendix A: Calculation of partial decay widths in the bound state approximation

In the default $D \leq 8$ calculation, the resonance states are obtained as bound state solutions in the model space of $D \leq 8$ fm. In a bound state approximation, the partial decay width $\Gamma_{I\otimes J'}$ of a resonance state for $^6\mathrm{He}(I^+)+\alpha(t)$ channels with the angular momentum coupling $[I\otimes J']_J$ can be estimated from the reduced width amplitude $y(a)$ of the corresponding channel at a channel radius a,

$$\Gamma_{I\otimes J'} = \frac{2ka}{F_l^2(ka)+G_l^2(ka)}\gamma^2(a), \quad \text{(A1)}$$

$$\gamma^2(a) = \frac{\hbar^2}{2\mu a}\left[ay(a)\right]^2, \quad \text{(A2)}$$

where F_l and G_l are the regular and irregular Coulomb functions, respectively, k is the momentum of inter-cluster motion in the asymptotic region, and μ is the reduced mass. $\gamma^2(a)$ is the so-called reduced width. l is the orbital angular momentum of the relative motion. In the present work, $y(a)$ are approximately calculated by using the overlap with the $^6\mathrm{He}(I^+)+\alpha(t)$ cluster wave function $\Phi^{[I\otimes J']_J}_{^6\mathrm{He}+\alpha(t)}(D=a)$ by means of the method proposed in Ref. [62] as,

$$ay(a) \approx \frac{1}{\sqrt{2}}\left(\frac{2\gamma}{\pi}\right)^{1/4}\left\langle \Psi^{J^\pi_k}\middle|\Phi^{[I\otimes J']_J}_{^6\mathrm{He}+\alpha(t)}(D=a)\right\rangle. \quad \text{(A3)}$$

[1] W. von Oertzen, M. Freer and Y. Kanada-En'yo, Phys. Rep. **432**, 43 (2006).

[2] Y. Kanada-En'yo and H. Horiuchi, Prog. Theor. Phys. Suppl. **142**, 205 (2001).

[3] Y. Kanada-En'yo, M. Kimura and A. Ono, PTEP **2012** 01A202 (2012).
[4] M. Ito and K. Ikeda, Rep. Prog. Phys. **77** (2014) 096301.
[5] S. Okabe, Y. Abe, and H. Tanaka, Prog. Theory. Phys. **57**, 866 (1977); S. Okabe and Y. Abe, Prog. Theor. Phys. **59**, 315 (1978); S. Okabe, Y. Abe, Prog. Theory. Phys. **61**, 1049 (1979).
[6] M. Seya, M. Kohno, and S. Nagata, Prog. Theor. Phys. **65**, 204 (1981).
[7] W. von Oertzen, Z. Phys. A **354**, 37 (1996); **357**, 355 (1997),
[8] W. von Oertzen, Nuovo Cimento **110**, 895 (1997).
[9] K. Arai, Y. Ogawa, Y. Suzuki and K. Varga, Phys. Rev. C **54**, 132 (1996).
[10] A. Dote, H. Horiuchi and Y. Kanada-En'yo, Phys. Rev. C **56**, 1844 (1997).
[11] Y. Ogawa, K. Arai, Y. Suzuki and K. Varga, Nucl. Phys. A **673**, 122 (2000).
[12] Y. Kanada-En'yo, H. Horiuchi and A. Dote, Phys. Rev. C **60**, 064304 (1999).
[13] N. Itagaki and S. Okabe, Phys. Rev. C **61**, 044306 (2000).
[14] N. Itagaki, S. Okabe and K. Ikeda, Phys. Rev. C **62**, 034301 (2000).
[15] N. Itagaki, S. Hirose, T. Otsuka, S. Okabe and K. Ikeda, Phys. Rev. C **65**, 044302 (2002).
[16] P. Descouvemont and D. Baye, Phys. Lett. **B505**, 71 (2001).
[17] P. Descouvemont, Nucl. Phys. **A699**, 463 (2002).
[18] Y. Kanada-En'yo and H. Horiuchi, Phys. Rev. C **66**, 024305 (2002).
[19] Y. Kanada-En'yo and H. Horiuchi, Phys. Rev. C **68**, 014319 (2003).
[20] M. Ito, K. Kato and K. Ikeda, Phys. Lett. B **588**, 43 (2004).
[21] W. von Oertzen and H. G. Bohlen, C. R. Physique **4**, 465 (2003).
[22] K. Arai, Phys. Rev. C **69**, 014309 (2004).
[23] M. Ito, Phys. Lett. B **636**, 293 (2006).
[24] M. Ito, N. Itagaki, H. Sakurai and K. Ikeda, Phys. Rev. Lett. **100**, 182502 (2008).
[25] M. Dufour, P. Descouvemont, and D. Baye, Nuc. Phys. A **836**, 242 (2010).
[26] M. Ito, Phys. Rev. C **83**, 044319 (2011).
[27] M. Ito, N. Itagaki and K. Ikeda, Phys. Rev. C **85**, 014302 (2012).
[28] Y. Kanada-En'yo, Phys. Rev. C **85**, 044320 (2012).
[29] K. Fujimura, D. Baye, P. Descouvemont, Y. Suzuki and K. Varga, Phys. Rev. C **59**, 817 (1999).
[30] Y. Kanada-En'yo, Phys. Rev. C **66**, 011303 (2002).
[31] S. Hamada, M. Yasue, S. Kubono, M. H. Tanaka and R. J. Peterson, Phys. Rev. C **49**, 3192 (1994).
[32] N. Soic *et al.*, Europhys. Lett. **34**, 7 (1996).
[33] N. Curtis, D. D. Caussyn, N. R. Fletcher, F. Marechal, N. Fay and D. Robson, Phys. Rev. C **64**, 044604 (2001).
[34] J. A. Liendo, N. Curtis, D. D. Caussyn, N. R. Fletcher and T. Kurtukian-Nieto, Phys. Rev. C **65**, 034317 (2002).
[35] N. R. Fletcher, D. D. Caussyn, F. Marechal, N. Curtis and J. A. Liendo, Phys. Rev. C **68**, 024316 (2003).
[36] N. Curtis *et al.*, Phys. Rev. C **70**, 014305 (2004).
[37] S. Ahmed *et al.*, Phys. Rev. C **69**, 024303 (2004).
[38] M. Milin *et al.*, Nucl. Phys. **A753**, 263 (2005).
[39] M. Freer *et al.*, Phys. Rev. Lett. **96**, 042501 (2006).
[40] H. G. Bohlen, T. Dorsch, T. Kokalova, W. von Oertzen, C. Schulz and C. Wheldon, Phys. Rev. C **75**, 054604 (2007).
[41] N. Curtis, N. I. Ashwood, M. Freer, T. Munoz-Britton, C. Wheldon, V. A. Ziman, S. Brown and W. N. Catford *et al.*, J. Phys. G **36**, 015108 (2009).
[42] D. Suzuki *et al.*, Phys. Rev. C **87**, no. 5, 054301 (2013).
[43] H.G. Bohlen, *et al.*, Nouvo Cimento A **111**, 841 (1998).
[44] H. G. Bohlen *et al.*, Phys. Atom. Nucl. **65**, 603 (2002).
[45] A.A. Korsheninnikov *et al.*, Phys. Lett. B 343, 53 (1995).
[46] M. Freer *et al.*, Phys. Rev. Lett. **82**, 1383 (1999).
[47] M. Freer *et al.*, Phys. Rev. C **63**, 034301 (2001) [Phys. Rev. C **64**, 019904 (2001)].
[48] A. Saito, *et al.*, Nucl. Phys. **A738**, 337 (2004); A. Saito, S. Shimoura, T. Minemura, Y. U. Matsuyama, H. Baba, N. Aoi, T. Gomi and Y. Higurashi *et al.*, Mod. Phys. Lett. A **25**, 1858 (2010).
[49] Z. H. Yang *et al.*, Phys. Rev. Lett. **112**, no. 16, 162501 (2014).
[50] F. Kobayashi and Y. Kanada-En'yo, Phys. Rev. C **86**, 064303 (2012).
[51] A. N. Kuchera *et al.*, Phys. Rev. C **84**, 054615 (2011) [Phys. Rev. C **85**, 069902 (2012)] [Phys. Rev. C **88**, no. 3, 039901 (2013)].
[52] Y. Kanada-En'yo and T. Suhara, Phys. Rev. C **85**, 024303 (2012).
[53] D. L. Hill and J. A. Wheeler, Phys. Rev. **89**, 1102 (1953); J. J. Griffin and J. A. Wheeler, Phys. Rev. **108**, 311 (1957).
[54] D. M. Brink, in Proceedings of the International School of Physics: Enrico Fermi, Course 36, edited by C. Bloch (Academic Press, New York, 1966).
[55] Y. Kanada-En'yo, H. Horiuchi and A. Ono, Phys. Rev. C **52**, 628 (1995).
[56] A. B. Volkov, Nucl. Phys **74**, 33 (1965).
[57] N. Yamaguchi, T. Kasahara, S. Nagata and Y. Akaishi, Prog. Theor. Phys. **62**, 1018 (1979); R. Tamagaki, Prog. Theor. Phys. **39**, 91 (1968).
[58] T. Suhara and Y. Kanada-En'yo, Prog. Theor. Phys. **123**, 303 (2010).
[59] Y. Suzuki and S. Hara, Phys. Rev. C **39**, 658 (1989).
[60] T. Kawabata *et al.*, Phys. Lett. B **646**, 6 (2007).
[61] T. Yamada, Y. Funaki, T. Myo, H. Horiuchi, K. Ikeda, G. Ropke, P. Schuck and A. Tohsaki, Phys. Rev. C **85**, 034315 (2012).
[62] Y. Kanada-En'yo, T. Suhara and Y. Taniguchi, PTEP **2014**, 073D02 (2014).
[63] W. Nortershauser, D. Tiedemann, M. Zakova, Z. Andjelkovic, K. Blaum, M. L. Bissell, R. Cazan and G. W. F. Drake *et al.*, Phys. Rev. Lett. **102**, 062503 (2009).
[64] G. Ewald *et al.*, Phys. Rev. Lett. **93**, 113002 (2004).
[65] A. Ozawa, T. Suzuki and I. Tanihata, Nucl. Phys. A **693**, 32 (2001).